Integrated Modeling Applied to the Terrestrial Planet Finder Mission

Andrew Kissil[a], Eug Kwack[a], Timothy Ho[a], Philip Dumont[a], Sandra Irish[b], Ichung Weng[c]
[a]Jet Propulsion Laboratory, California Institute of Technology, 4800 Oak Grove Drive, Pasadena, CA, USA 91109-8099
[b]Goddard Space Flight Center, Greenbelt, MD, USA 20771
[c]Swales Aerospace, 5050 Powder Mill Rd, Beltsville, MD, USA 20705

ABSTRACT

Integrated Modeling is currently being used to assess the feasibility of a baseline design concept (pre-phase A), developed for the Coronagraph version of the Terrestrial Planet Finder (TPF) mission. This design concept incorporates many challenging design elements for a space-born observatory: including a monolithic 8 by 3.5 meter elliptical primary mirror; a 12 meter long deployable secondary mirror support structure; as well as a 14 meter long deployable, tensioned-membrane, V-groove sunshield. Unprecedented thermal and dynamic stability is required by this flight system to allow observation of enough contrast between planets and their parent stars. This stringent performance requirement necessitates a balanced system, designed to optimize the various interacting disciplines: optical, thermal, structural & control. To support design feasibility studies, a MATLAB-environment-based integrated modeling tool (IMOS: Integrated Modeling of Optical Systems) was employed for analyzing the end-to-end system performance for typical in-orbit maneuvers. Our integrated modeling goal is to use a single model definition file to specify the thermal, structural, and optical modeling and analysis parameters, improving results accuracy, configuration control and data management. In working towards that goal, we have had parallel efforts in IMOS capability development, as well as design concept modeling and analysis. Typical system performance metrics studied include the relative motions of the optical elements, as well as the deformation of individual optics, decomposed into best-fitting Zernike polynomials.

Keywords: TPF, coronagraph, planet-finder, telescope, deployable, sun-shield, solar-sail, large-optics, CTE

1. INTRODUCTION

The primary goal of the Terrestrial Planet Finder (TPF) Project is to detect and characterize earth-sized planets orbiting nearby stars. TPF is planning on flying two complementary observatories: a Coronagraph-based telescope to be launched around 2016, and a formation-flying Interferometer to be launched around 2020. This paper addresses design feasibility studies conducted for the TPF-Coronagraph Mission, and the on-going integrated modeling tool development intended to support these and similar studies.

1.1. System Description

Previously, we had developed a Minimum Mission Design configuration, which addressed the minimum science requirements. For this cycle, we are developing a configuration concept, called Flight Baseline cycle 1 (FB1), which addresses the full mission science goals. The FB1 system is composed of the combination of the Spacecraft Assembly and the Science Payload Assembly, as shown in Fig. 1.1.1. The Spacecraft Assembly is composed of the Spacecraft Bus (including reaction wheel assembly, propulsion tanks & ancillary equipment), as well as the Sunshield, Solar Array & Solar Sail. The Science Payload Assembly consists of the Optical Telescope Assembly (OTA), as well as the Payload Support Assembly, which includes the instruments (Starlight Suppression, Planet Detection & Characterization, General Astrophysics, etc) and thermal enclosure, designed to thermally isolate the instruments & primary mirror (PM).

The telescope, comprised of the primary and secondary mirrors and intermediate support structure, is an off-axis Cassegrain-type design, with a 12 m separation between the primary and secondary mirrors. The primary mirror is a monolithic light-weighted (front & back face-sheets with honeycomb core) 8 m by 3.5 m elliptical glass mirror (0.25 m overall thickness), made from Ultra-Low Expansion (ULE®) glass, and the secondary mirror is another light-weighted ULE® mirror, 0.9 m by 0.4 m in size. The combination produces a F/17.5 beam, with F-number considered along the

major axis. The secondary mirror is thermally isolated (as is the primary), and is mounted on an actuated hexapod, giving six degree of freedom motion control. The secondary mirror assembly sits on the end of a deployable tower, which is constructed of M55J/954-3 carbon fiber reinforced polymer (CFRP) composite material, having three folding (hinged & latched) joints. The secondary support tower connects to the Aft Metering Structure (same CFRP material), which supports the primary mirror. The tertiary mirror (M3), also part of the OTA, is a flat fold mirror which sits near the base of the tower, is heated, and also has 3 dof of motion control (piston, tip & tilt).

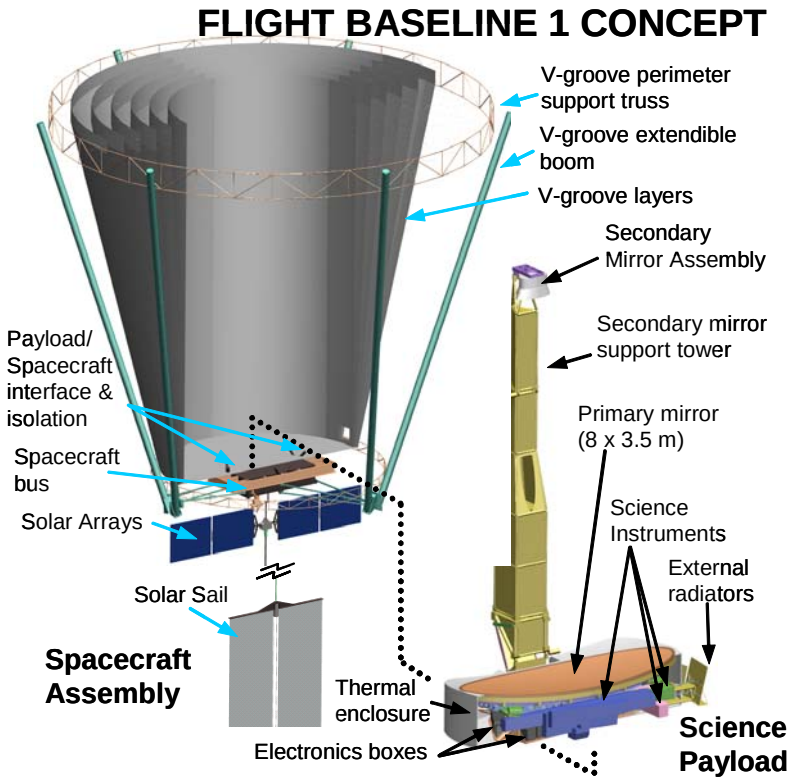

Fig. 1.1.1. Fully Deployed Observatory

The primary mirror is kinematically mounted (3 point attachment at the back of the mirror) to its support structure, the Aft Metering Structure (AMS), by three bipods. The AMS also supports the secondary mirror tower, and the combination of the AMS and the tower provide metering between the primary and secondary mirrors. The AMS is mounted to the Payload Support Structure (PSS). The primary mirror, the AMS and the instrument box are all housed within a common thermal isolation enclosure, which is intended to maintain a relatively constant temperature of near room temperature. The secondary mirror is also housed in its own thermal enclosure, while the support tower temperature is currently allowed to passively reach equilibrium, without active control. However, control may be added if need arises.

The FB1 system design allows for limited active motion compensation, using the secondary mirror, tertiary mirror, fine steering mirror (FSM), and a deformable mirror (DM). The secondary mirror is mounted on a hexapod-type actuator, which can control all six rigid-body degrees of freedom. The secondary mirror rigid-body motion can be controlled with feedback provided by a metrology system for response frequencies less than approximately 1 Hz. This will allow compensation for tower distortions due to slow changes in thermal environment after slew maneuvers. Higher frequency responses, such as responses to reaction wheel disturbance, cannot be compensated by the secondary mirror hexapod system, without a great deal of design effort and expense. The FSM is used in the pointing control system, and the DM is used to compensate for pseudo-static primary mirror distortions. The possibility of a coarse DM is also being investigated.

2. STRUCTURAL MODEL DESCRIPTION

2.1. Overall Model Description

The combined FB1 system Finite Element Model (FEM) is composed of two main assemblies: the Spacecraft Assembly, and the Science Payload Assembly. Fig. 2.1.1 shows a view of the Combined System model for the deployed observatory, and Fig. 2.1.2 shows a view of the Science Payload FEM by itself. The OTA, which is a subassembly of the Science Payload Assembly, was modeled by GSFC, and the rest of the system was modeled by JPL. You can see in the upper half of Fig. 2.1.1 that the Science Payload FEM is located within the v-groove sunshield.

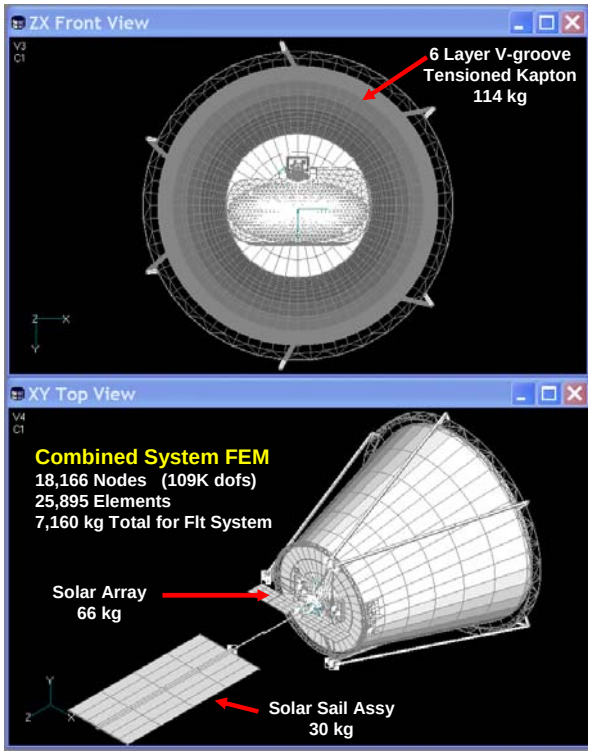

Fig. 2.1.1. FB1 Combined System Finite Element Model

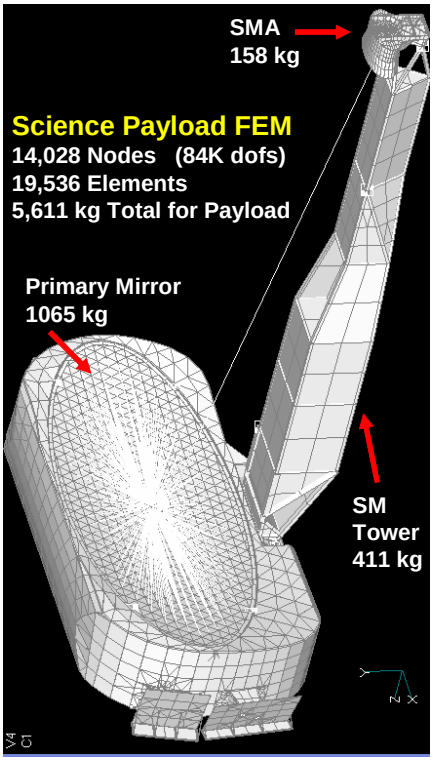

Fig. 2.1.2. FB1 Science Payload FEM

Fig.s 2.1.1 and 2.1.2 also list the vital model statistics, to give a sense of the model size and complexity. Enough model detail was added to adequately capture the major contributors to system performance. At the same time, great effort was spent toward minimizing the model size, in order to make analysis manageable, especially in regard to the integrated structural-thermal analysis.

The major assumptions or idealizations made in the FB1 modeling are the following: no hinges, latches or fittings were explicitly modeled; no temperature dependent properties were modeled (except for the primary mirror, as will be discussed later); uniform properties were assumed for like materials (once again, except for the primary mirror); lumped and smeared masses were used to represent non-structural hardware. Also, the tensioned membranes of the v-groove sunshield and solar sail were modeled using a linearized representation of the geometric stiffening due to the pre-load, as described in section 2.3 of Ref 1. Currently, we are assuming a perfectly uniform distribution of the tensioning stress, and future studies will address the effects of deviations from this ideal state: such as the effects of membrane-wrinkling and other non-uniformities in preload. The current approach used for this pre-phase A model was to capture a representative dynamic characterization with an ample distribution of modes.

Fig. 2.1.3 shows a top view of the Payload Support Assembly (PSA) FEM. The OTA attaches to the PSA to form the Science Payload. Fig. 2.1.4 shows the PSA without the thermal isolation enclosure. The thermal enclosure has a mass of 479 kg, and, by the way, is about the size of a standard school bus. The Payload Support Structure (PSS), identified in Fig. 2.1.4, is the workhorse of this assembly, supporting all of the instruments, as well as the OTA, and thermal enclosure. The PSS has a mass of 368 kg. The instrument models are generally just place-holders, since their structural details have not been worked out yet, but they do have representative mass and stiffness, allowing overall system performance feasibility to be evaluated. In the upper right corner of Fig. 2.1.4, are two passive radiators, with the rightmost being the colder one, which is used by the detectors.

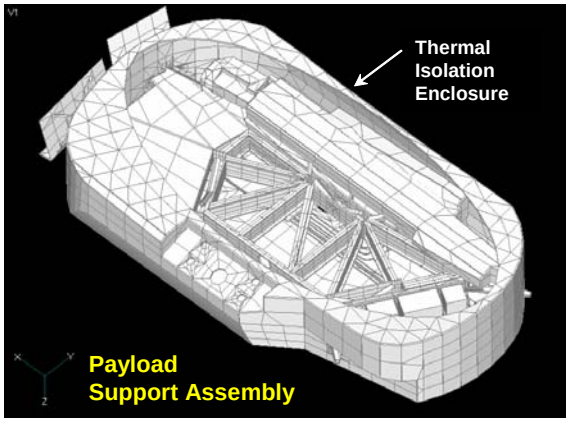

Fig. 2.1.3. FB1 Payload Support Assembly FEM

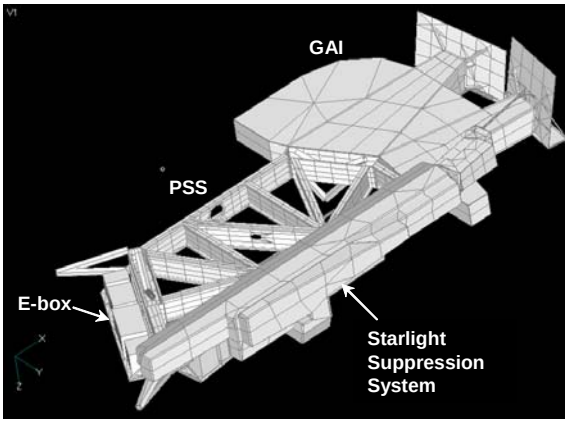

Fig. 2.1.4. FB1 Payload Support Assembly without Enclosure

2.2. Primary Mirror Model

The current FB1 primary mirror design concept is constructed using a light-weighted, monolithic ULE® glass blank that is elliptical in shape, with an 8m major diameter, a 3.5m minor diameter, and a depth of 0.25m. The construction is a honeycomb sandwich, with a segmented core: the front and back face-sheets are fused to the core structure. The nominal core design has hexagonal cells (0.129 meters flat-flat) with a cell wall thickness of 1.5mm.

We have three different models of the same primary mirror design, with each tailored for a specific analysis purpose. A low-fidelity model, comprised of a single-layer of plate elements formed on a curved surface, is used for trade studies. A mid-fidelity model (shown in Fig. 2.2.1) is constructed of a combination of plate and solid elements: plate elements are used to represent the front and back face-sheets, as well as outer side-walls and solid elements are used to represent the mirror core. The mid-fidelity model is used primarily for integrated analysis, and is good for overall dynamic and thermal distortion analysis. However, the mid-fidelity model cannot capture local distortion effects at the core-cell level, such as surface print-through. GSFC is using a very detailed high-fidelity model of the mirror, which is composed entirely of plate elements, to evaluate detailed stresses, as well as the effects of print-through. This High-fidelity model is unwieldy for trade and Monte Carlo studies, having almost 200K nodes and 300K elements. Fig. 2.2.2 shows a plot of the high-fidelity model mirror core elements.

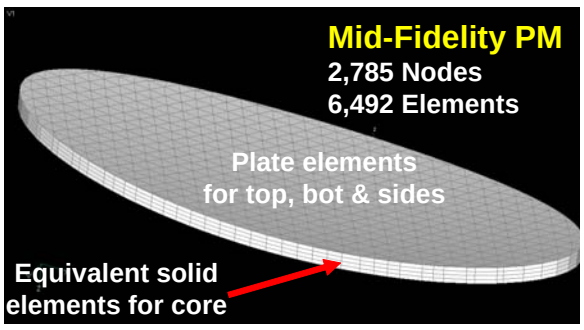

Fig. 2.2.1. Mid-Fidelity Primary Mirror Model

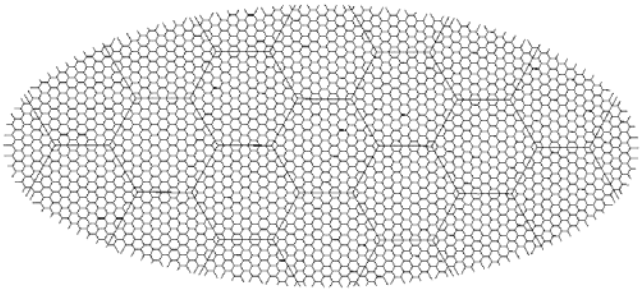

Fig. 2.2.2. High-Fidelity Primary Mirror Model Core

3. ANALYSIS DESCRIPTION

3.1. Integrated Analysis Approach

We are using an integrated modeling approach of using models as consistent as possible between the different analysis disciplines. A common CAD definition is used throughout the design cycle development. Also, the structural model finite element mesh is used for developing the integrated thermal model. Of course, no restriction is made on the meshing for separate thermal trade study models, and for studies of solution convergence with mesh size, etc. However, the integrated models for the flight system structural and thermal disciplines were restricted to have consistent meshes, minimizing errors introduced in mapping results from one analysis phase to the next: e.g. temperature results from thermal analysis to temperature boundary condition for displacement computations. This issue is especially critical when dealing with the ultra-stable system performance requirements, as levied in the FB1 error budget.

One insidious example illustrating this point was encountered recently when transmitting temperature results from the TMG thermal analysis to the structural analysis phase. We encountered this problem even though we had consistent thermal and structural model meshes. Since TMG computed temperature results for elements, rather than for nodes, we used TMG to do the mapping of temperatures from elements to nodes, within the same model. Although the computed nodal temperatures ranged from approximately -150 to +20 deg C for the conditions investigated, we were more concerned with the temperature stability when slewing the observatory from one position to the next, for which the critical temperature changes were in the neighborhood of 1e-5 deg C. Unfortunately, small interpolation/extrapolation errors were introduced by TMG during the element temperature to nodal temperature mapping process. These small errors are magnified greatly when computing the delta-temperatures. We noticed unacceptable jaggedness in the transient nodal delta-temperature time histories: whereas, the element delta-temperature time-histories were very smooth. The approach we selected for solving this error propagation problem was to do the element temperature to nodal temperature mapping outside of TMG, in MATLAB, using a more stable averaging method. An alternative would have been to work with element temperatures in the structural analysis.

In making the consistent mesh restriction, we are consciously taking a hit on optimal meshing for a particular discipline, with respect to computational time and results accuracy needed. In other words, we accept that some analyses may take longer than they would take when modeled conventionally. However, computer speeds have advanced to the point where the delay is acceptably small: especially, in light of the increased accuracy benefit of having consistent meshes.

We are working toward making the transition between disciplines as seamless as possible, and our IMOS (Integrated Modeling of Optical Systems, see Ref. 2) development goals are consistent with this vision. Currently, IMOS development is transitioning to a new database approach (see Ref. 4), which frees up large chunks of memory that would otherwise be tied up with model information, allowing larger problems to be solved more rapidly. Also, wherever possible, compiling of code is being used to speed the processing. The thermal and structural models can share a common base model, with extra nodes or elements being added for a particular discipline. This approach minimizes results mapping and model translation errors.

3.2. Thermal Analysis

Early-on it was believed that one of the tall tent-poles limiting system performance might be telescope thermal stability during a dither-type of observation maneuver, performed for planet detection. We are currently base-lining the usage of dithering for speckle removal, to help increase our contrast sensitivity. This was one of the reasons for choosing a cocoon-type of configuration for the v-groove sunshield. The DM can be used to compensate for WFE after a slew to acquire a new target star, or after a roll about the bore-sight direction to take advantage of the primary mirror long axis with respect to planet orbit position. However, the DM cannot be used after a dither-roll maneuver, since doing so would change the speckle pattern, hindering speckle removal. The stability after a dither-roll is therefore a critical factor for system performance. Currently, we are planning on having three roll angles, 60 degrees apart, with a 30 degree dither about each, as illustrated in Fig. 3.2.1. The Sun is excluded from the right side (as viewed), because of the presence of radiators used for passive cooling.

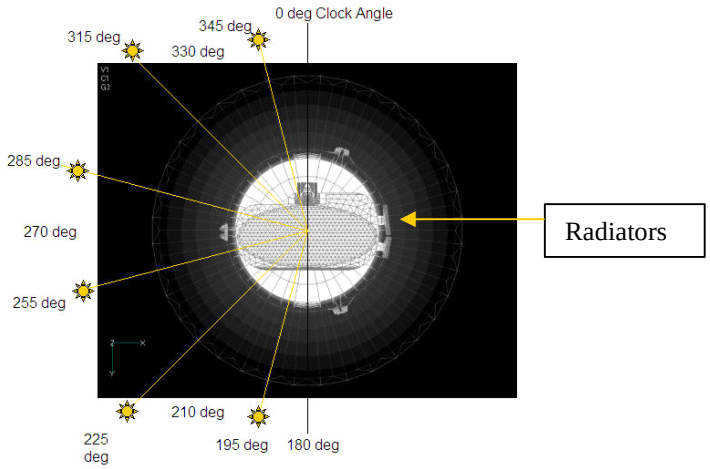

Fig. 3.2.1. Roll & Dither Sun Positions, Viewed Along Bore-Axis from Target

So far, we have analyzed two dither cases: one from the 195 to 225 deg position, and the other from the 255 to 285 degree position, as shown in Fig. 3.2.1. The worst case (larger temperature changes) was found to be the 195 to 225 deg dither, because of the proximity of the cold radiator (which cools the detectors) to the Sun at the 195 deg position. We have not yet analyzed cases with the Sun behind the telescope, which will introduce shadowing of the solar array. We will be addressing these issues in the near future.

3.3. Overall Structural Distortion Analysis

The changes in temperature caused by dithering the telescope (roll about the bore-axis) 30 degrees from one roll angle to another (e.g. 195 to 225 deg) induce distortions of the optical elements, as well as in the hardware that support the optics. We used IMOS to do the structural distortion analysis caused by these thermal perturbations, for both steady-state and transient conditions. The thermal transients were handled as pseudo-static load cases for the structural analysis. Temperature dependent material properties were not generally incorporated in the analyses thus far, but will be addressed in future studies. We did, however, address temperature dependence of the primary mirror CTE, as will be discussed below. IMOS provides some very useful leverage for the thermal distortion analysis in the fact that multiple load cases (as used in Monte Carlo studies) can be easily generated and analyzed, and the MATLAB environment provides a method of generating complex variations of material properties, such as simulating CTE variability. Also, using IMOS naturally gives access to sensitivity matrices (see below) that would not otherwise be readily available.

The way we normally do the thermal distortion analysis in IMOS is to generate a temperature-to-load matrix **[R]**, which produces a load vector (generating equivalent thermal expansion) when multiplied by a temperature vector. The usual static equation of motion is the following:

$$\mathbf{K}\,\{u\} = \{p\} \tag{3.3-1}$$

where **[K]** is the stiffness matrix, **{u}** is the nodal displacement vector, and **{p}** is the load vector, and

$$\{p\} = [R]\,\{t\} \tag{3.3-2}$$

Then **{p}** in Eq. (3.3-1) can be replaced by the product **[R] {t}**, in Eq. (3.3-2), where **{t}** is the delta-temperature vector, producing the following:

$$\{u\} = [K]^{-1}\,[R]\,\{t\} \tag{3.3-3}$$

If we consider **[B]** to be a mapping matrix from the general displacement vector to particular displacements or pointing orientations of interest **{v}**, then

$$\{v\} = [B]\,\{u\} \tag{3.3-4}$$

and substituting Eq. (3.3-4) into Eq. (3.3-3) yields

$$\{v\} = [B]\,[K]^{-1}\,[R]\,\{t\} \tag{3.3-5}$$

If we also have an optical sensitivity matrix **[C]** that maps particular displacements to system OPD wave-front error **{w}**, then we can pre-multiply Eq. (3.3-5) as follows:

$$\mathbf{\{w\} = [C]\,\{v\} = [C]\,[B]\,[K]^{-1}\,[R]\,\{t\}} \tag{3.3-6}$$

We can compute the $\mathbf{[C]\,[B]\,[K]^{-1}\,[R]}$ product separately to examine the sensitivity of system performance to changes in temperature. This is sometimes useful for determining temperature sensor or heater placement.

We have also performed a variation of the standard thermal distortion analysis by factoring out the element CTEs. Working directly with element CTEs avoids problems encountered with using equivalent grid point temperature changes, such as when elements of dissimilar materials join at a common node. Eq. (3.3-2) can be transformed into the following equation by factoring out the element CTEs:

$$\mathbf{\{p\} = [S]\,\{cte\}} \tag{3.3-7}$$

where **[S]** is a CTE-to-load mapping matrix, which has the temperature vector already embedded in it.

Eq. (3.3-2) can be replaced with Eq. (3.3-7) in a similar fashion to the above derivation of Eq. (3.3-6), giving:

$$\mathbf{\{w\} = [C]\,\{v\} = [C]\,[B]\,[K]^{-1}\,[S]\,\{cte\}} \tag{3.3-8}$$

Eq. (3.3-8) is useful for evaluating the sensitivity of system performance to variations of element CTEs.

3.4. Primary Mirror CTE Variability

We also used IMOS to explore the effects of CTE variability within the primary mirror. CTE variability in the metering structure is also of interest, and will be looked at, but is not considered a tall tent-pole, since we have adjustability built into the system, which can compensate. Variability of CTE in the primary mirror, however, can have a direct limiting effect on our performance capability.

Analyses were performed for both a uniform CTE assumption, as well as for the variable CTE. The uniform assumption is of course simpler and faster, but we determined that it is not an adequate assumption to make, and can lead to non-conservative performance predictions. We will show, by analysis, that it is necessary to take manufacturer predictions of glass-boule CTE variability into account to get a more accurate performance evaluation. Furthermore, we plan on extensive testing to validate these models. The modeling is further complicated by the fact that the FB1 primary mirror is so large that 92 separate pieces of glass are needed for construction of the blank. There are 23 segments, with each segment composed of 4 separate pieces: two face-sheets (top and bottom), and two boules stacked and fused to form the core. On the other hand, having multiple pieces of glass will tend to average-out the influence of CTE variation with individual boules on overall performance: the smaller the regions (fraction of total) of random variation, the smaller their net effect will be on system performance.

Our approach to analyzing CTE variability was to perform a standard Monte Carlo simulation, in which the element CTEs were varied according to pre-selected functions. There has been extensive CTE measurement done by the glass manufacturer in an effort to characterize the variation within a typical boule of glass, as well as the variation from boule to boule. Based on these finding, a set of CTE specifications were assembled for the Technology Development Mirror (TDM), which is being used to demonstrate the feasibility and performance for certain technologies anticipated to be key to the TPFC system development. Table 3.4.1 outlines the CTE specifications that were presented at the TDM PDR.

Table 3.4.1 TDM Blank CTE Specifications from PDR

INITIAL MIRROR CTE TOLERANCES		
No.	**Description**	**Tolerance (ppb/C)**
1	Weighted Blank Average	+/- 10
2	Core Segment Axial Gradient	+/- 10
3	Core Segment Radial Range	< 15
4	Max Core Segment-Segment Average Delta	< 10
5	Face Plate Axial Gradient	+/- 5
6	Face Plates Pt-to-Pt Difference	< 5
7	(Face Plate Average) - (Core Segment Average)	+5 to +15

We used four major functions for describing the variation of CTE within each of the 92 regions: bias, side to side (2 directions), radial, and axial. Parameters controlling the magnitude of these variations were given a "flat-top" random variation, having limits consistent with the TDM specifications given in Table 3.4.1. For our Monte Carlo study, we generated 1000 load cases (vectors of element CTEs). Fig. 3.4.1 shows a color contour plot, illustrating the CTE distribution for one of the 1000 cases analyzed. The segmentation, and variation within segment regions, is discernable.

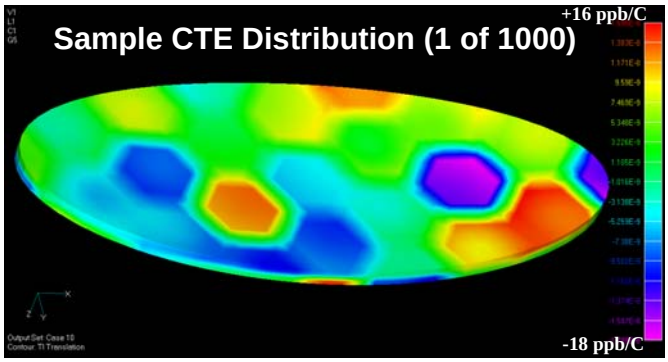

Fig. 3.4.1. Contours of PM CTE for 1 of 1000 Cases Generated

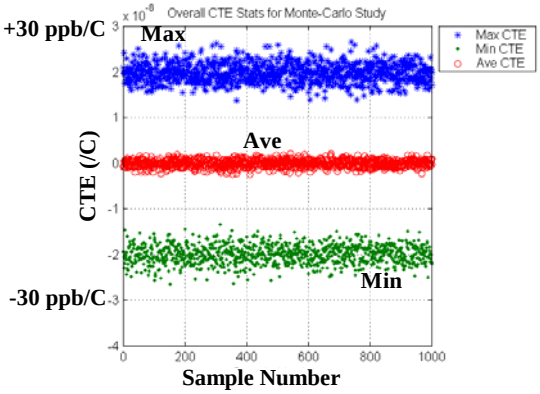

Fig. 3.4.2 Overall CTE Statistics for PM

4. ANALYSIS & PERFORMANCE RESULTS

4.1. Thermal Analysis Results

Fig. 4.1.1 shows the steady-state temperature (deg C) contours for various parts of the Science Payload, for the case of having the Sun in the 195 deg Position, as indicated in Fig. 3.2.1. The temperature values indicated would not really change much for any of the other roll positions, given the number of significant digits seen here. Given that, these temperatures are representative for any roll position (analyzed thus far). We can see in the upper left and lower right quadrants of this figure that most of the structure inside the thermal enclosure is maintained near room temperature, as intended. The radiators, which protrude from the thermal enclosure, reach the coldest temperature present: -203 deg C. The secondary mirror is also maintained near room temperature. The temperature of the secondary mirror support tower, however, is allowed to reach passive equilibrium: the mid-span of the tower reaches -100 deg C. The primary mirror, having heaters behind it and around its sides, shows the expected temperature variation, with the center of the top surface being the coldest. It is of interest to note that we see a temperature variation of about 6 deg C for the primary mirror: with the gradient primarily going from the hot back-side toward the cooler front-side.

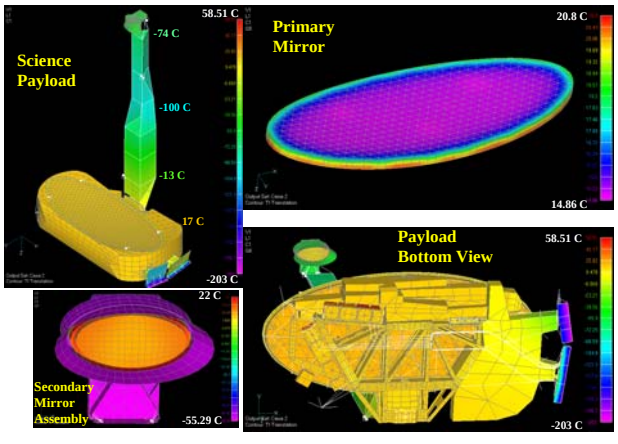

Fig. 4.1.1. Temperatures (deg C) with Sun at the 195 deg

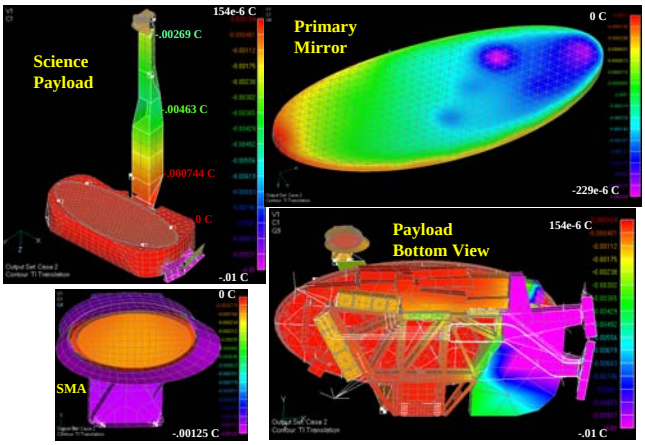

Fig. 4.1.2. Contours of Delta-Temperatures (195-225 Dither)

Fig. 4.1.2 shows a color contour plot of the temperature changes (C) exhibited as a result of dithering (30 deg roll about bore-axis) from the 195 deg position to the 225 deg position (see Fig. 3.2.1). We chose to show the 195-225 deg dither case, since this turned out to be the worst case, analyzed so far. These are steady-state results: i.e. both start and finishing temperature results were generated using steady-state analysis. We can see that the largest temperature changes occurring in the telescope assembly take place at the mid-span of the secondary support tower: there is a change of approximately 5e-3 deg C. The largest changes overall occur at the radiator, as would be expected. However, we can also see that large temperature changes also occur in the radiator support structure. This heat sink even influences the nearest PM bipod, since we can clearly see in the upper right plot that the mount point is printing through. We will show, however, that the primary mirror distortion is dominated by the average changes in front to back temperatures, across the mirror.

Fig.s 4.1.3 & 4.1.4 show the transient response (deg C) of the primary mirror over a 24 hour period (x-axis) after a 30 deg dither maneuver (195-225). Fig. 4.1.3 traces the average primary mirror temperature, and Fig. 4.1.4 shows its average change in front-to-back delta temperature. On both plots, the steady-state results are shown on the right edge. We can see that the transient temperatures are converging nicely toward the steady-state, even though different solution methods were used for the two approaches. We can also observe that the time constant is such that the temperatures level out roughly 10 to 15 hours after the dither event.

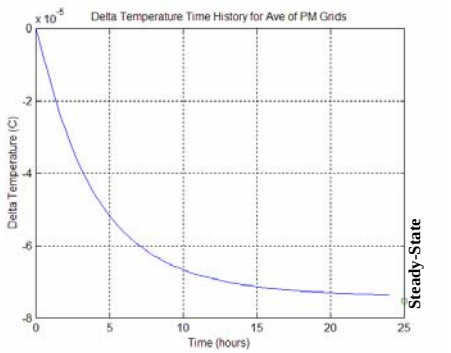

Fig. 4.1.3. Ave PM Temperature Change (195-225 Dither)

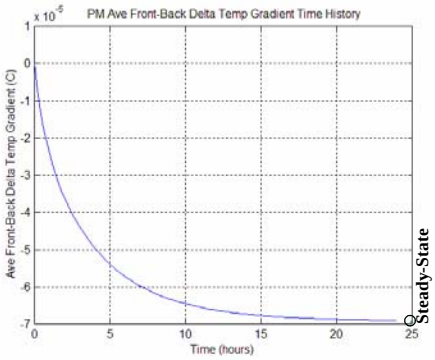

Fig. 4.1.4. Ave Change of PM Front-Back Delta-Temperature

4.2. Structural Analysis Results

Fig.s 4.2.1-4.2.4 show the transient response of the propagated OPD WFE caused by the distortion of the primary mirror, due to the thermal disturbance of a 30 deg dither (195-225). For computing the WFE, we used a sensitivity matrix, as described in Eq. (3.3-6). These results are for the case of uniform CTE assumed for the primary mirror. The aberrations were decomposed using best-fitting elliptical Zernikes (1st 15 terms). The x-axis is time (hours) after the dither, and the y-axis is RMS WFE (m). The steady-state responses are also shown in these plots, indicated by the symbols along the right edge. The error budget requirement level is indicated by the symbols in the upper right corner of each plot. We can see that the responses are well within the error budget requirements (by > factor of 10).

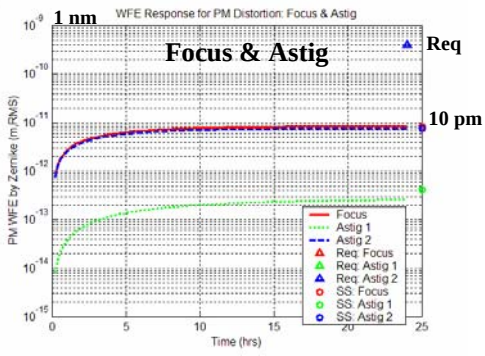

Fig. 4.2.1. Focus & Astig WFE Response (195-225 Dither)

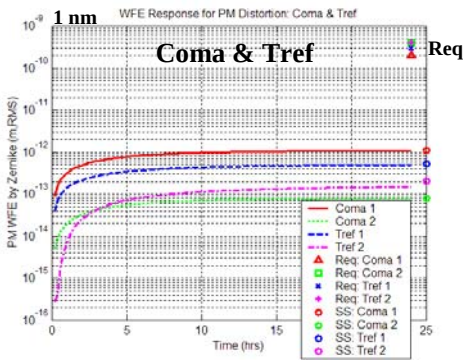

Fig. 4.2.2. Coma & Tref WFE Response (195-225 Dither)

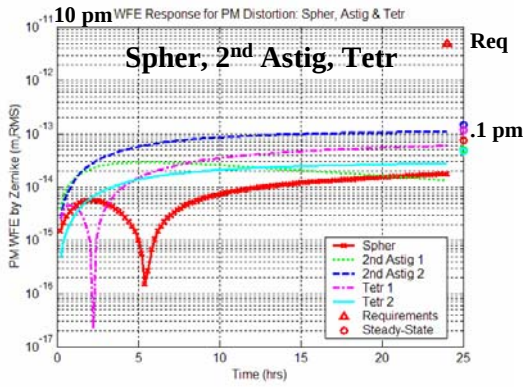

Fig. 4.2.3. Spher, 2nd Astig, Tetr WFE Response (195-225 Dither)

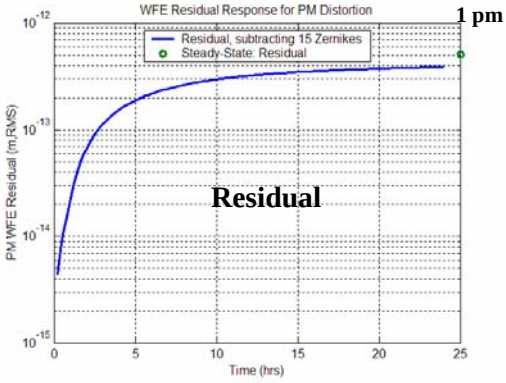

Fig. 4.2.4. Residual WFE Response (195-225 Dither)

Fig. 4.2.5 is a OPD WFE map resulting from the distortion of the primary mirror, taken as a snapshot 24 hours after a 30 deg dither (195-225). We can see that the WFE is dominated by a circular focus, which was hypothesized to be caused by a change in front-to-back delta-temperature across the mirror. The circular focus decomposes primarily into elliptical Zernike focus and astigmatism. Fig. 4.2.6 is a cross-plot of the elliptical focus and astigmatism as a function of the change in front-to-back delta-temperature. We can see that the elliptical focus and astigmatism have very near linear variations with the change in front-to-back delta-temperature. A separate analysis was run in which a pure change in front-to-back delta-temperature was the only disturbance present, and the response matched the slope shown in Fig. 4.2.6, corroborating our hypothesis that this effect was causing the observed response for the dither.

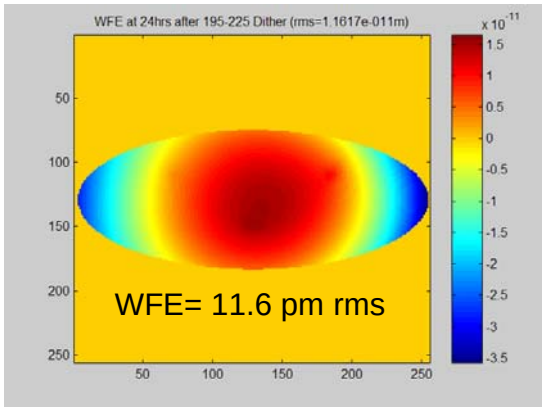

Fig. 4.2.5. WFE Map at 24 hrs after Dither (195-225)

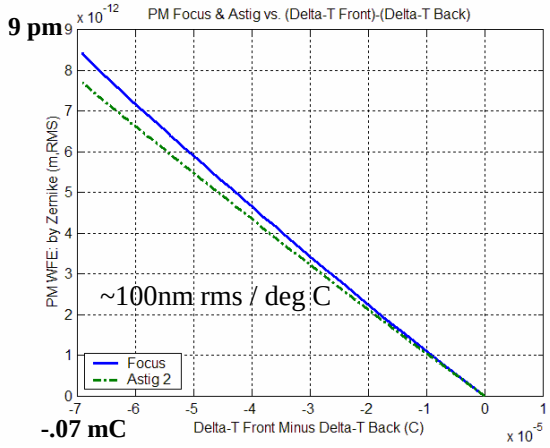

Fig. 4.2.6. Focus & Astig vs. Delta PM Front-Back Delta-Temp

Fig.s 4.2.7 & 4.2.8 show the open-loop relative rigid body motions of optics, with respect to the primary mirror, for thermal disturbance due to a 30 deg dither (195-225). Transient responses are shown over a 24 hour period after the dither event. Also, steady-state responses are indicated by the symbols on the right edge of each plot. Error budget requirement levels are indicated by the triangles plotted near the right edge: these were derived from beam-walk effects rather than aberrations, which are negligible. Fig. 4.2.7 is a plot of the secondary mirror motion relative to the primary, given in terms of despace & decenter, and Fig. 4.2.8 is a plot of the motions of M3, M4 (1st 2 folds) and the coronagraph, with respect to the PM. We can see in all cases shown that the computed responses are within the error budget. It is also important to note that the secondary mirror motion is within budget, even without compensating its motion with its active mount. Once again, these results are for assuming a uniform CTE in the primary mirror model.

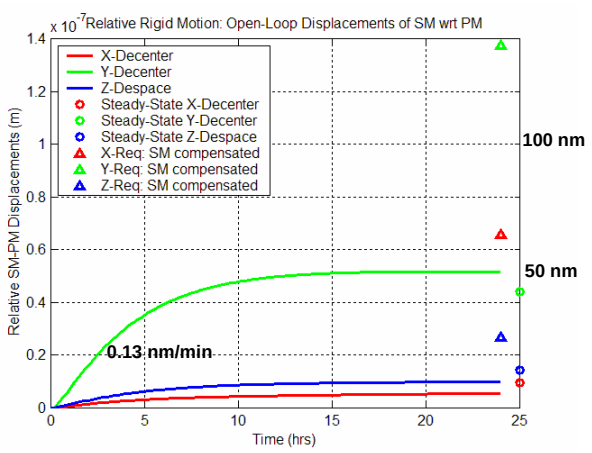

Fig. 4.2.7. Secondary Mirror Motion due to Dither (195-225)

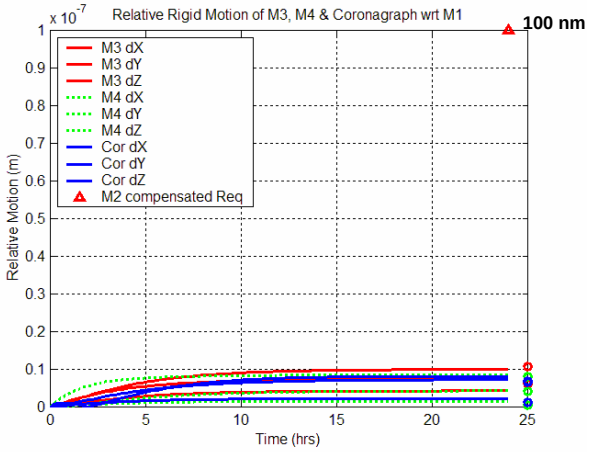

Fig. 4.2.8. M3, M4 & Coronagraph Motion for Dither (195-225)

Fig.s 4.2.9 & 4.2.10 show the results obtained for the Monte Carlo PM CTE study, using steady-state 30 deg dither (195-225) temperature results. As described in section 3.4, the mirror CTE was given random variations in accordance with pre-defined functions, and the resulting propagated OPD WFE performance was monitored. The x-axis is the elliptical Zernike term (4-15), and the y-axis is the RMS WFE (m). Fig. 4.2.9 shows the predicted response for the expected CTE variations, as indicated by the "+" and "*" markers, representing sampled maximum and 3-sigma responses, respectively. The triangles indicate the response when a uniform CTE is used. The error budget requirements are indicated by the "o" markers. We can see that our predicted responses are well within the error budget. It is also apparent that the uniform CTE assumption under-predicts the WFE for all but the lowest Zernike terms.

Fig. 4.2.10 shows what happens when we also introduce an estimate for the CTE temperature dependence in the PM, as well as the previously modeled CTE variations. A conservative estimate was made for a linear variation of CTE with temperature: 2ppb/C/C, based on Corning ULE® spec-sheet data. In Fig. 4.2.10, we see an increase by factor of 2 in the WFE for the low-order Zernikes: focus and astigmatism. The predicted response, however, is still well within the error budget. We will follow-up with analysis using material properties based on temperature dependent look-up tables.

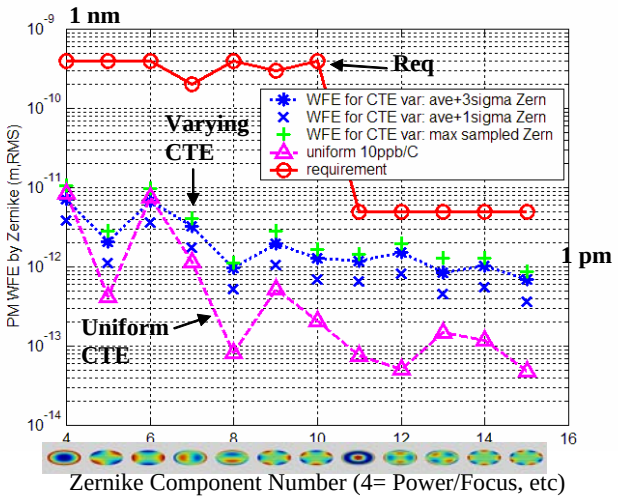

Fig. 4.2.9. WFE Response with PM CTE Var (195-225 Dither)

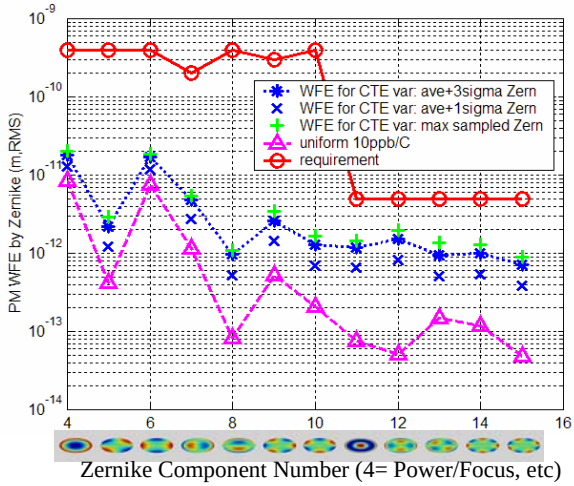

Fig. 4.2.10. WFE Response with PM CTE Var & Temp Depend

We could also expect to get significant improvement (i.e. reduced WFE) by positioning mirror segments, based upon in-situ CTE measurements of the as-built individual segment blanks, before assembly of the whole mirror blank. A similar approach has already been demonstrated to work in the SUBARU and GEMINI mirrors, and was analytically shown to help significantly in the TPF Minimum Mission study (Ref. 3). Additional improvement could be obtained with selection and placement (before fusion) of front-back face-sheet pairs, based on CTE measurement data.

5. CONCLUSION

Our current studies demonstrate the design feasibility of the Full Mission, Flight Baseline 1 design concept, based on the computed responses to thermal disturbances. We are still continuing with our investigations, using more realistic modeling assumptions, and additional environmental conditions. The modeling tools have proved to be adequate so far, and we are continuing with tool development to increase processing speed, model size capability and overall reliability.

Acknowledgments - The research described in this paper was carried out at the Jet Propulsion Laboratory, California Institute of Technology, under a contract with the National Aeronautics and Space Administration.

REFERENCES

1. A. Kissil, et al, *Structural Modeling for the Terrestrial Planet Finder Mission,* SPIE 5528A4, August 5, 2004.
2. JPL, *Integrated Modeling of Optical Systems User's Manual*, Release 5.0, JPL Pub. 98-12, Rev. A, Feb. 2000.
3. M. Levine, et al, *Terrestrial Planet Finder Coronagraph Minimum Mission Baseline Design and Analysis Report,* JPL 28535, April 22, 2004.
4. G.J. Moore, et al, *Multidisciplinary Analysis for Large-Scale Optical Design,* SPIE 5528A13, August 5, 2004.